ELSEVIER

Bioinspired, heredity-derived hierarchical bulk multifunctional copper alloys

Peijian Shi [a,b,†], Zhe Shen [a,†], Hongguang Wang [c,†], Zhi Li [d], Yejun Gu [d,e], Yi Li [a], Jie Yan [b], Zhongze Lin [a], Mingyang Wang [a], Yinpan Yang [a], Chunyan Ling [f], Biao Ding [a], Na Min [g], Jianchao Peng [g], Junhua Luan [b], Tengshi Liu [a], Weili Ren [a], Zuosheng Lei [a], Yangtao Zhou [h], Yi Liu [i], Ningning Liang [i], Peter A. van Aken [c], Yang Ren [j], Yunbo Zhong [a,*], C.T. Liu [b,*], Huajian Gao [k,*], Yuntian Zhu [b,*]

[a] State Key Laboratory of Advanced Special Steel, Shanghai Key Laboratory of Advanced Ferromletallurgy, School of Materials Science and Engineering, Shanghai University, Shanghai, China
[b] Department of Materials Science and Engineering, Hong Kong Institute for Advanced Study, College of Science and Engineering, City University of Hong Kong, Hong Kong, China
[c] Max Planck Institute for Solid State Research, Stuttgart, Germany
[d] Institute of High Performance Computing, Agency for Science, Technology and Research, Singapore
[e] Department of Mechanical Engineering, Whiting School of Engineering, Johns Hopkins University, Baltimore, USA
[f] Department of Advanced Design and Systems Engineering, City University of Hong Kong, Hong Kong, China
[g] Laboratory for Microstructures, Shanghai University, Shanghai, China
[h] Shenyang National Laboratory for Materials Science, Institute of Metal Research, Chinese Academy of Sciences, Shenyang, China
[i] School of Materials Science and Engineering, Nanjing University of Science and Technology, Jiangsu, China
[j] Department of Physics, City University of Hong Kong, Hong Kong, China
[k] School of Mechanical and Aerospace Engineering, Nanyang Technological University, Singapore

Bioinspired hierarchical design demonstrates a promising microstructural solution to circumvent multiple intricate property trade-offs in artificial materials. However, it remains extremely challenging to tailor structural hierarchies feasibly and synthetically, particularly for bulk materials. Here, a counterintuitive strategy is reported–exploring multiscale microstructural heredities for highly-developed dendritic hierarchies in as-cast bulk alloys. During optimized thermomechanical processing, we carefully control these dendrites to be progressively deformed, elongated, aligned and refined, rather than completely destroying them as in conventional alloy processing paradigms. As such, a hierarchical fibrous lamellar (HFL) structure–resembling those of shell and bamboo–is controllably designed in a technologically-important CuCrZr alloy. This innovative HFL design promotes multiple synergetic micro-mechanisms with sequential multiscale interactions and salient biomimetic attributes, thereby affording exceptional multifunctionality, especially record-high strength–ductility–conductivity combination. At more fundamental levels, multiple previously inaccessible deformation and reinforcement mechanisms are activated by exploiting the HFL structure-enabled complex internal stress condition. They perform and interact at multi-length-scales from intense diversified

* Corresponding authors.
E-mail addresses: Zhong, Y. (yunboz@staff.shu.edu.cn), Liu, C.T. (chainliu@cityu.edu.hk), Gao, H. (huajian.gao@ntu.edu.sg), Zhu, Y. (y.zhu@cityu.edu.hk).
† These authors contributed equally to this work.

https://doi.org/10.1016/j.mattod.2023.11.003

dislocation trapping, massive stacking-fault proliferation, 9R-phase-assited nano-twinning, self-buffering shear bands to ever-intensified hetero-deformation-induced hardening. These scenarios even create superior, strain-rate-tolerant dynamic properties far exceeding conventional homogeneous-structured counterparts. Dendrites exist ubiquitously, yet generally undesirable, in metallic materials, whereas our 'bioinspired, heredity-derived' strategy counterintuitively utilizes them, realizing unprecedented high figure-of-merit multifunctionality.

Introduction

The quest for safety-critical and energy-saving engineering technologies necessitates the advancement of high-performance multifunctional materials [1–11]. Unfortunately, the required critical properties are often mutually exclusive; for example, elevating the strength often sacrifices the ductility, toughness, conductivity and even thermostability of engineering materials. Traditional approaches, such as grain refinement, can improve one or two aspects of material performance, but possess rather limited ability to evade trade-offs among multiple mutually exclusive properties in a single material. Natural materials, such as bone, shell and wood, have found their unique ways around multiple property trade-off paradoxes [7–15]. Nature's wisdom resides in its exquisite, self-assembled hierarchical architectures that allow for efficient all-length-scale functional adaptation, thereby leading to today's outstanding multifunctionality. In light of this, microstructural hierarchies are thus increasingly being introduced into a wide range of engineering materials [1–15]. Despite great promise, it has been extremely challenging to tailor structural hierarchies feasibly and synthetically, at multiple length scales, particularly for bulk materials [7–15]. Moreover, the associated techniques replicating nature's designs are not readily scalable to the established and affordable industrial processing routes [7–15].

To address these challenges with a bio-inspired design strategy, here we report an innovative strategy of exploring multiscale microstructural heredities for highly developed dendritic hierarchies in as-cast bulk alloy materials [16]. By exploiting this 'bioinspired, heredity-derived' strategy, a hierarchical fibrous lamellar (HFL) structure is controllably designed with length scales spanning five to six orders of magnitude. Of particular note is that, this distinctive HFL structure promotes multiple synergistic reinforcement micromechanisms characterized by sequential, topologically varied multiscale interactions and salient biomimetic attributes. These complementary merits successfully evade multiple property trade-offs in a widely-studied/applied Cu-1.0wt%Cr-0.1wt%Zr alloy [17–21] (Supplementary Note 1), leading to simultaneously high electrical conductivity [~80 % International Annealed Copper Standard (IACS)], yield strength (~655 MPa), uniform elongation (~6.8 %), thermal stability, anti-shearing damage, casting flaw tolerance, wear resistance, impact toughness and even ultrahigh-speed tensile properties. In particular, the exceptional strength–ductility–conductivity combination enables our HFL-reinforced materials to outperform all reported Cu-1.0wt%Cr-0.1wt%Zr and its derived or alike alloy systems to date, while the record-breaking properties are superior over those of other kinds of state-of-the-art bulk copper alloys. Taken together, among copper alloys, such appreciable and diversified properties are unprecedented–making our HFL materials truly multifunctional (Supplementary Note 2)–which is of great application importance, but to our knowledge does not exist in their traditional homogeneous-structured counterparts.

Apart from high figure-of-merit multifunctionality, a grander impact of the bioinspired, heredity-derived strategy is that many distinct, previously unattainable technological advantages become available. First, in as-cast bulk alloys, dendrites are common but generally undesirable because of the attendant variety of casting flaws (e.g., composition segregation) and often disastrous cracking during downstream plastic processing. Thus, in conventional processing, these developed dendrites need to be fully eliminated by costly and lengthy high-temperature homogenization annealing (and other complicated treatment) [18–22]. However, we counterintuitively utilize the dendrites, greatly reducing the manufacturing costs in terms of energy, time and infrastructure requirements, without sacrificing other critical attributes. Second, the developed dendrites, being natural structural precursors, provide an *in-situ* bionic access to the structural hierarchy design across multiple length scales. Thus, more advanced hierarchical structures can be obtained feasibly by solidifying or additive manufacturing higher-order dendritic precursors. This scenario extends great opportunities to explore hitherto uncharted territory in the multifunction-property profile. Furthermore, our processing techniques adopted are compatible with current industrial practices, whereby our demonstrated strategy should be readily extendable to other alloy systems because dendrites exist ubiquitously in diverse as-cast metallic materials.

To showcase the bioinspired, heredity-derived innovative strategy, three types of Cu-1.0wt%Cr-0.1wt%Zr samples were fabricated. The first one, an as-cast base sample, was produced by industrial continuous casting with high production efficiency, while the second and third specimens were prepared by processing the first specimen with high-temperature homogenization annealing, equal-channel angular pressing (ECAP) and ageing/recrystallization annealing, as well as with direct extrusion, rotary swaging and ageing/recrystallization annealing, respectively.

Fig. 1a shows optical microscopy (OM) images, revealing that the first as-cast bar sample has highly-branched Cu-rich dendrites varying from the millimetre to micron scales. Enlarged scanning-electron microscopy (SEM) and energy-dispersive X-ray spectroscopy (EDS) characterizations (Fig. 1b) show that the interdendritic regions, spanning from the micron to nanoscale, comprise numerous inferior Cr-rich flake segregations and some rod-shaped eutectic phases. Therefore, the industrial continuous casting has solidified a highly developed dendritic structure encompassing multiple length scales, as further confirmed in

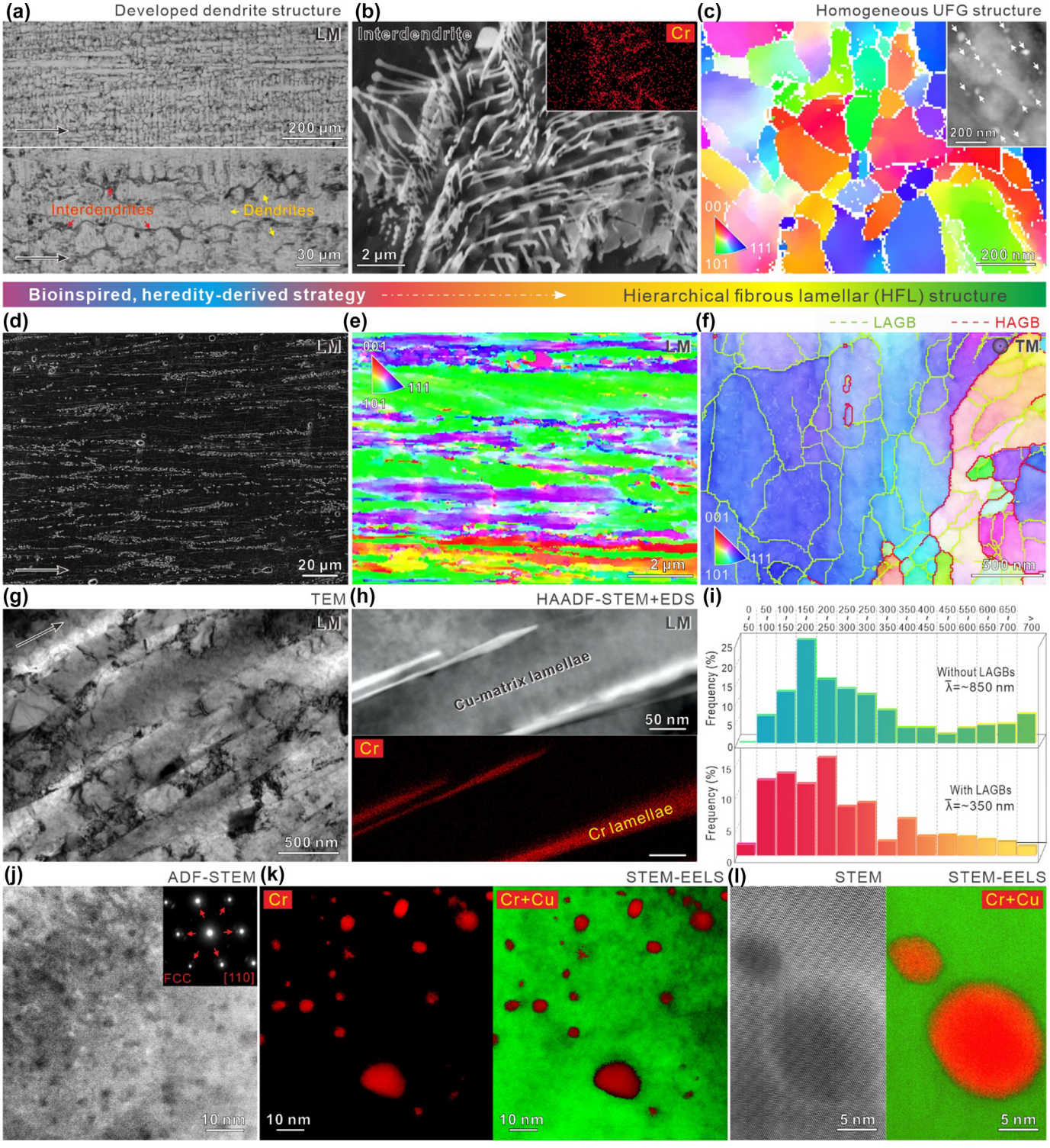

FIG. 1

Bioinspired, heredity-derived HFL architecture. a, b, OM and SEM images of the as-cast CuCrZr sample. The inset shows the SEM-EDS mapping of Cr segregation. **c,** EBSD inverse pole figure (IPF) image of the UFG ECAP sample serving here as the reference material. The inset shows the corresponding HAADF-STEM image, and white arrows mark dense intergranular precipitates. **d–l,** Designed HFL sample. **d–h,** SEM, EBSD IPF, EBSD IPF, TEM and HAADF-STEM as well as EDS mapping images. **f,** EBSD IPF image identifying widespread LAGBs. LAGBs and HAGBs are marked with green and red lines, respectively. **i,** Grain-size distribution of HAGBs (upper) and HAGBs + LAGBs (lower). **j,** ADF-STEM image of nanoprecipitates. **k,** STEM-EELS mapping of Cr and Cu + Cr elements. **l,** Atomic-resolution STEM image and STEM-EELS mapping of bimodal precipitates. The arrows in (a, d, g) indicate the longitudinal direction. All LM and TM refer to longitudinal and transverse microstructures, respectively.

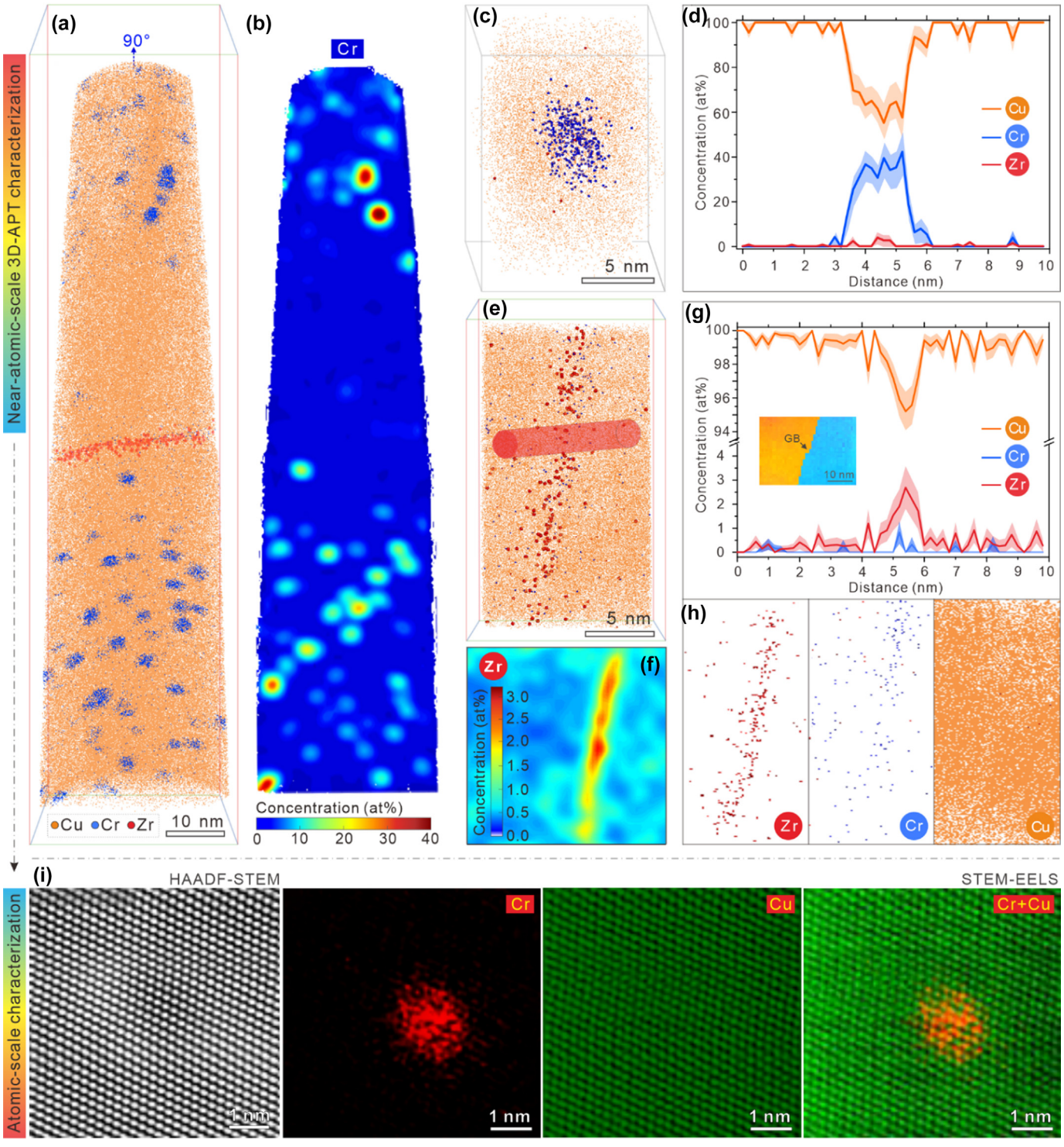

FIG. 2

Multimodal nanoprecipitates and interface element segregation. a, Near-atomic-scale APT reconstruction map showing multimodal Cr-rich precipitates in the copper matrix and the Zr-element distribution at grain boundaries. **b,** Two-dimensional contour colour profile of the Cr concentration in (a) with 90° rotation. Enlarged atom map showing a Cr-rich precipitate (**c**) and a grain boundary decorated with Zr segregation (**e**). One-dimensional composition profile of the Cr-rich precipitate (**d**) and cylinder crossing the grain boundary (**g**). GB refers to the grain boundary. **f,** Two-dimensional contour colour profile of the Zr concentration in (**e**). **h,** Atom maps of Zr, Cr and Cu at a grain boundary. **i,** Atomic-level HAADF-STEM image and atomic-resolution STEM-EELS mapping of a cluster.

transverse microstructure examinations (Supplementary Figs. 1a, 2a). Compared to the as-cast multiscale specimen, the second specimen exhibits distinctly different microstructures. After lengthy high-temperature homogenization annealing, we observe a heavily degraded dendritic structure and undissolved Cr segregations with a spheroidized particle appearance (-

Supplementary Fig. 2). Further ECAP and recrystallization annealing generate ultrafine grains with an average size of ~250 nm, as revealed by electron-backscatter diffraction (EBSD; Fig. 1c). Thus, these processing treatments enable a completely new and homogeneous ultrafine-grained (UFG) structure rather than certain heredity for the as-cast hierarchical one. Here, some undissolved Cr segregations were presumed to be severely broken during ECAP, thus forming part of the grain-boundary nanoprecipitates [21], as observed in the high-angle annular dark-field (HAADF) scanning transmission-electron microscopy (STEM) inset (Fig. 1c).

Different from the second sample, a multiscale HFL structure was tailored in the third sample–alike to those of shell and bamboo–spanning across multiple length scales (see Fig. 1d–h). To access the bioinspired HFL architecture, we deliberately explored multiscale microstructural heredities for the as-cast developed dendritic hierarchies (Supplementary Fig. 1), rather than completely breaking them as usual. Systematic microstructure characterizations reveal that the multiscale inheritance is particularly assisted by the progressive thermoplastic deformation, elongation and alignment of the hierarchical as-cast microstructure along the bar-length axis, as well as the concurrent adjustment and refinement along the short axis (as detailed in Supplementary Figs. 1, 3–5 and Supplementary Note 3). Thus, as schematically illustrated in Fig. 3a and b, the non-annealed, and surviving, dendritic hierarchies successfully work as an effective structural precursor. It makes the heredity-derived structure correspondingly exhibit a 3D hierarchical architecture in terms of the formed fibrous lamellar size, category and topology distribution (Fig. 1d–h, Supplementary Figs. 4, 5).

As further illustrated in Fig. 1i, the final CuCrZr rod shows a distinct multimodal distribution of the lamellar thickness. In addition, due to low annealing temperature and insufficient time, the CuCrZr rod exhibits profuse low-angle grain boundaries (LAGBs; 5~15°) at the high proportion of ~72.4%, as revealed by both longitudinal (LM) and transverse (TM) microstructures (Fig. 1e, f). The LAGBs substantially subdivide the coarse-grained lamellae with high-angle grain boundaries (HAGBs), resulting in the lamellar thickness decreasing from the HAGB-controlled ~850 nm to the LAGB-dominated ~350 nm (Fig. 1i). Moreover, dense nanoscale precipitates were detected in the Cu-rich lamellae, as shown in the ADF-STEM image (Fig. 1j). Near-atomic-resolution STEM electron energy loss spectroscopy (EELS) mapping (Fig. 1k, l) reveals that there are primarily two size ranges of nano-precipitates. Both of them are coherent with the Cu matrix and display the same face-centred cubic (FCC) crystal structure as the matrix (inset, Fig. 1j and Supplementary Fig. 6). The larger precipitates (10~14 nm) constitute a lower proportion of ~12%, while the finer predominant precipitates (3~6 nm) feature higher coherence degree with a lattice misfit of ~0.33%. When revisiting the thermomechanically-processed substructures, it was revealed that the bimodal precipitates resulted from dynamic precipitation during extrusion (Supplementary Fig. 7) and ageing precipitation during annealing (Fig. 1j–l), respectively [23].

Near-atomic-scale 3D atom probe tomography (3D-APT) characterization was also conducted (Fig. 2a, b), which further revealed abundant near-spherical precipitates with a density of ~$1.42 \times 10^{23}\,m^{-3}$. By utilizing proximity histograms calculated from the isoconcentration surface, the precipitate composition was captured, showing that all precipitates, irrespective of their size or shape, are chemically similar, and their composition averaged over all morphologies is 35.79 ± 6.22 at% Cr, 63.89 ± 6.25 at % Cu and 0.13 ± 0.13 at% Zr (Fig. 2c, d). Further atomic-scale STEM-EELS mapping (Fig. 2i) detected a few fully coherent, much smaller solute clusters (1~2 nm). Acting as the precipitate

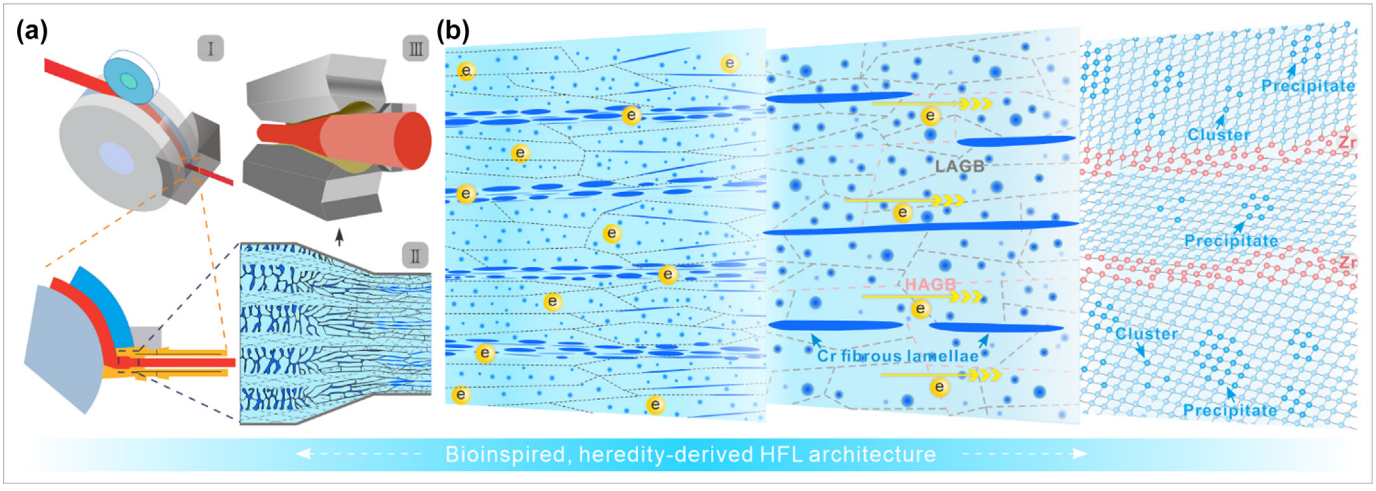

FIG. 3

Schematic diagrams of the processing route and the resulting heredity-derived multiscale HFL microstructure, respectively (a and b). In **a**, the two insets I and III show continuous extrusion and rotary swaging, respectively. The inset II illustrates the design philosophy that we deliberately explored multiscale microstructural heredities for the as-cast developed dendritic hierarchies, rather than completely breaking them as usual. The multiscale inheritance is assisted by the progressive thermoplastic deformation, elongation and alignment of the hierarchical as-cast microstructure along the bar-length axis, as well as the concurrent adjustment and refinement along the short axis. Together with tailored annealing parameter, the bioinspired, heredity-derived HFL architecture is successfully realized with length scales spanning across five to six orders of magnitude in **b**.

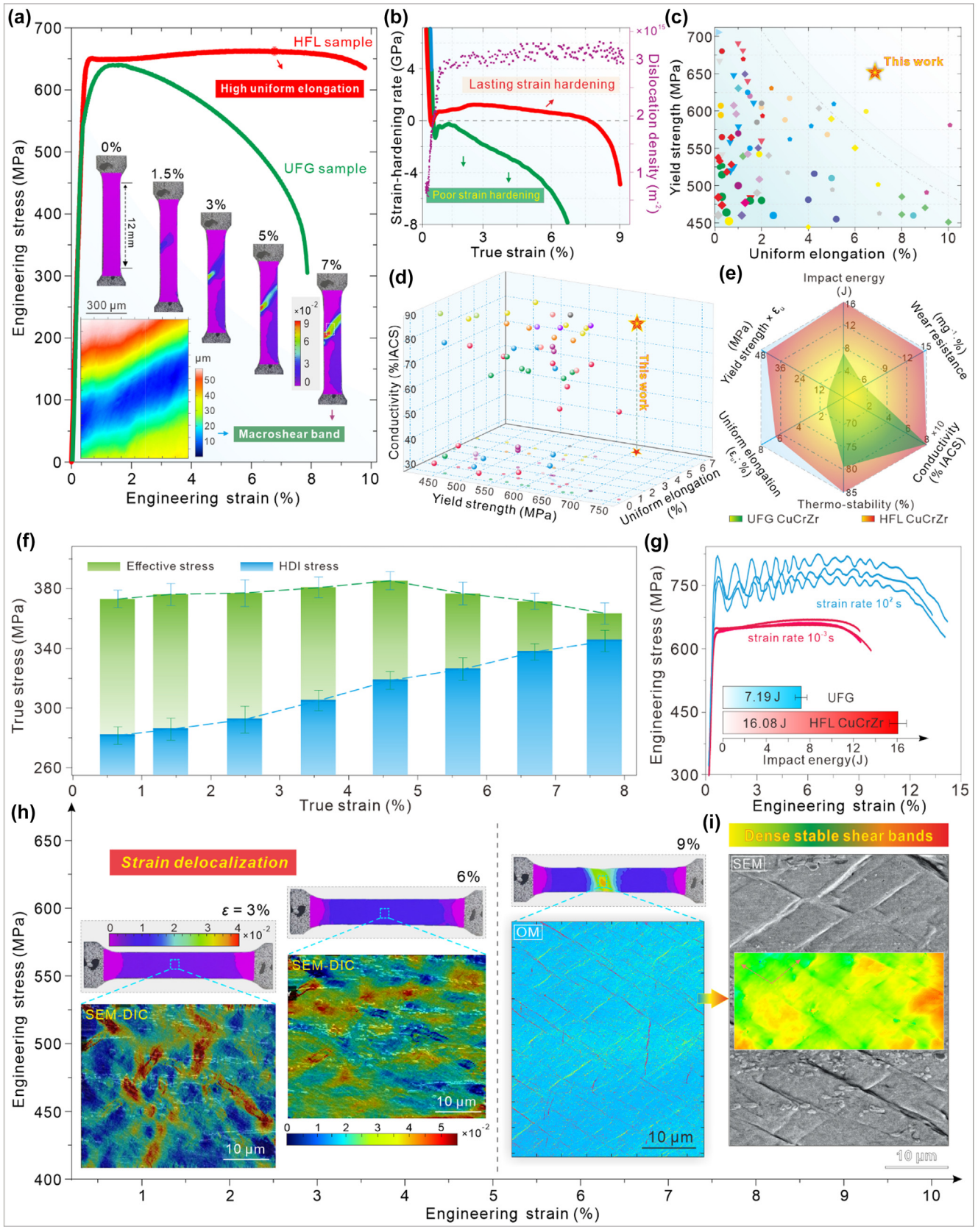
(a)
HFL sample
High uniform elongation
UFG sample
0%
1.5%
3%
5%
7%
12mm
300 μm
μm
Macroshear band
Engineering stress (MPa)
Engineering strain (%)
(b)
Lasting strain hardening
Poor strain hardening
Strain-hardening rate (GPa)
Dislocation density (m⁻²)
True strain (%)
(c)
This work
Yield strength (MPa)
Uniform elongation (%)
(d)
This work
Conductivity (%IACS)
Yield strength (MPa)
Uniform elongation (%)
(e)
Impact energy (J)
Wear resistance
Conductivity (%IACS)
Thermo-stability (%)
Uniform elongation
Yield strength × ε_u
UFG CuCrZr
HFL CuCrZr
(f)
Effective stress
HDI stress
True stress (MPa)
True strain (%)
(g)
strain rate 10² s
strain rate 10⁻³ s
7.19 J
UFG
16.08 J
HFL CuCrZr
Impact energy(J)
Engineering stress (MPa)
Engineering strain (%)
(h)
Strain delocalization
ε = 3%
6%
9%
SEM-DIC
SEM-DIC
OM
10 μm
10 μm
10 μm
Engineering stress (MPa)
Engineering strain (%)
(i)
Dense stable shear bands
SEM
10 μm

precursor, they manifest as a local fluctuation and weak aggregation of Cr atoms. Moreover, an unexpected Zr spike at grain boundaries is identified in both one-dimensional concentration profile and two-dimensional Zr concentration map of APT datasets (Fig. 2e–h). The concentration at the Zr spike was determined to be 2.88 ± 0.89 at% (Fig. 2g), which is approximately four times higher than the nominal Zr content (~0.70 at%) of the present material. This Zr-enriching behaviour may rationalize the detected Zr deficiency within precipitates (Fig. 2d). Further STEM-EDS observations also confirm this abnormal Zr behaviour, which prevails mostly at HAGBs (Supplementary Fig. 8). The excess energy of LAGBs is usually a fraction of that of HAGBs, whereby the latter hence can provide a much higher driving force for element enrichment or segregation [24].

Fig. 4a displays the tensile behaviour of the HFL specimen. To emphasize the salient effectiveness of the bioinspired, heredity-derived strategy, the mechanical response of UFG ECAP specimen was also measured for comparison. The UFG microstructure endows the ECAP counterpart with a high yield strength of ~580 MPa, but coming with disappointingly low uniform elongation (~1.5%) (Fig. 4a). The sharp ductility sacrifice can be attributed to the poor dislocation accumulation ability of ultrafine grains (Supplementary Fig. 9d) due to the easy dislocation annihilation around UFG boundaries [25–28]. Thus, the potent hardening mechanism mediated by dislocations is lost, resulting in inferior uniform elongation. In addition, severe plastic deformation applied to the CuCrZr materials for tailoring UFG structures is generally achieved by ECAP and/or certain atypical processes, such as dynamic plastic deformation at liquid-nitrogen temperatures [18–22]. Although some obtained results are impressive (irrespective of their inferior uniform elongation), these techniques are not feasible for bulk production to satisfy the large-size requirements of railway contact wires, for example, which are in great demand (Supplementary Note 4).

In comparison, our bioinspired, heredity-derived engineering strategy delivers strong and favourable message for overcoming these drawbacks. Compared to its high-strength UFG counterpart, the tailored HFL material exhibits a higher yield strength of ~655 MPa, simultaneously concomitant with far larger uniform elongation up to ~6.8% (Fig. 4a). This property trend successfully breaks the long-standing strength–ductility trade-off prevailing in traditional high-strength CuCrZr materials [18–22]. Of particular interest is that, the exceptional strength–ductility combination, especially the ultrahigh uniform elongation, outperforms those of all recorded Cu-1.0wt%Cr-0.1wt%Zr and its derived or alike alloy systems to date (Fig. 4c). The unusual property combination also highlights that our HFL material features a salient ability to absorb energy during plastic deformation, indicative of superior toughness (as quantitatively indicated by the product of yield strength and uniform elongation; Supplementary Fig. 10). Additionally, it was noted that at an equivalent or higher yield-strength level, the reported CuCrZr alloys show poor and even negligible uniform elongation (Fig. 4c), resembling the property trend in our high-strength ECAP specimen due to their similar UFG trait [29–39]. The comparable structure and property features thus make it reasonable to use our ECAP UFG sample as the baseline for comparison in this study.

To reveal the atomic mechanisms for the exceptional yield strength, 3D discrete dislocation dynamics (DDD) and molecular dynamics (MD) simulations were conducted (see Supplementary Note 5). It was uncovered that the achieved ultrahigh yield strength (~655 MPa) mainly comes from precipitation strengthening (~280 MPa) and grain-boundary strengthening (~237 MPa). Differing from those reported high-strength CuCrZr alloys [29–31], numerous LAGBs (instead of HAGBs) in our HFL materials dominate the appreciable grain-boundary strengthening.

To understand mechanisms underpinning the surprisingly high uniform elongation, we performed multiscale digital image correlation (DIC) characterizations for the HFL specimen and the UFG one for comparison. The inset of Fig. 4a reveals that the UFG counterpart, after yielding, undergoes rapid local "necking" instability, and the necking deformation primarily affords the measured tensile strain. Additionally, the necking area comes with the formation of microcracks (Supplementary Fig. 9a–c). These adverse situations inevitably limit practical applications. However, at the same focusing scale, the HFL material exhibits widespread uniform deformation behaviour (see Fig. 4h), which matches well with the measured excellent uniform elongation (~6.8%). Further high-resolution SEM-DIC probing (Fig. 4h) did not find any local necking or microdamage throughout the uniform-deformation process, and in contrast, revealed a favourable strain-delocalization incident. After the lasting uniform deformation, a localized plastic deformation occurs, yet propagating unexpectedly in two directions, leading to a wider necking area (Fig. 4i). More strikingly, this atypical necking almost withstands the loading stress, resulting in only a weak, sluggish stress drop (Fig. 4a). This trend is distinctly different from sharp stress collapse popular in our UFG and other reported high-strength CuCrZr counterparts [29–39].

FIG. 4

Superior mechanical properties and distinctive deformation behaviours. a, Tensile curves of both UFG and HFL samples. The insets show in situ DIC observations for tensile deformation as well as confocal laser OM observations for the macroscopic SB of the UFG sample. **b,** Corresponding strain-hardening curves of the two samples and evolution of the dislocation density of the HFL sample. **c,** Yield strength versus uniform elongation of the HFL sample compared to those of previously reported CuCrZr materials (with the same or nearly the same composition as our material). **d,** Yield strength and uniform elongation versus conductivity compared to those of previously reported CuCrZr materials (with the same or nearly the same composition as our material). To ensure the rationality and accuracy of these data, a few overestimated properties measured by small-scale tensile samples are not included in c and d according to these Refs. [52,53]. **e,** Multiple property values or trends of the UFG and HFL samples. The wear resistance is expressed by the reciprocal of the wear weight loss. Thermostability refers to the ratio of the hardness after annealing at 550 ℃ for 3 h to the hardness before annealing. **f,** Associated evolution of both HDI stress and effective stress. **g,** Ultrahigh-speed and quasi-static tensile curves of HFL samples. The inset shows the impact energy of UFG and HFL CuCrZr samples. **h,** Multiscale coupled in-situ DIC observations for tensile deformation of the HFL sample. **i,** Coloured OM and SEM images showing dense, stable SBs. The inset in the right image shows a confocal laser scanning microscopy image, further displaying and confirming the prevailing SBs.

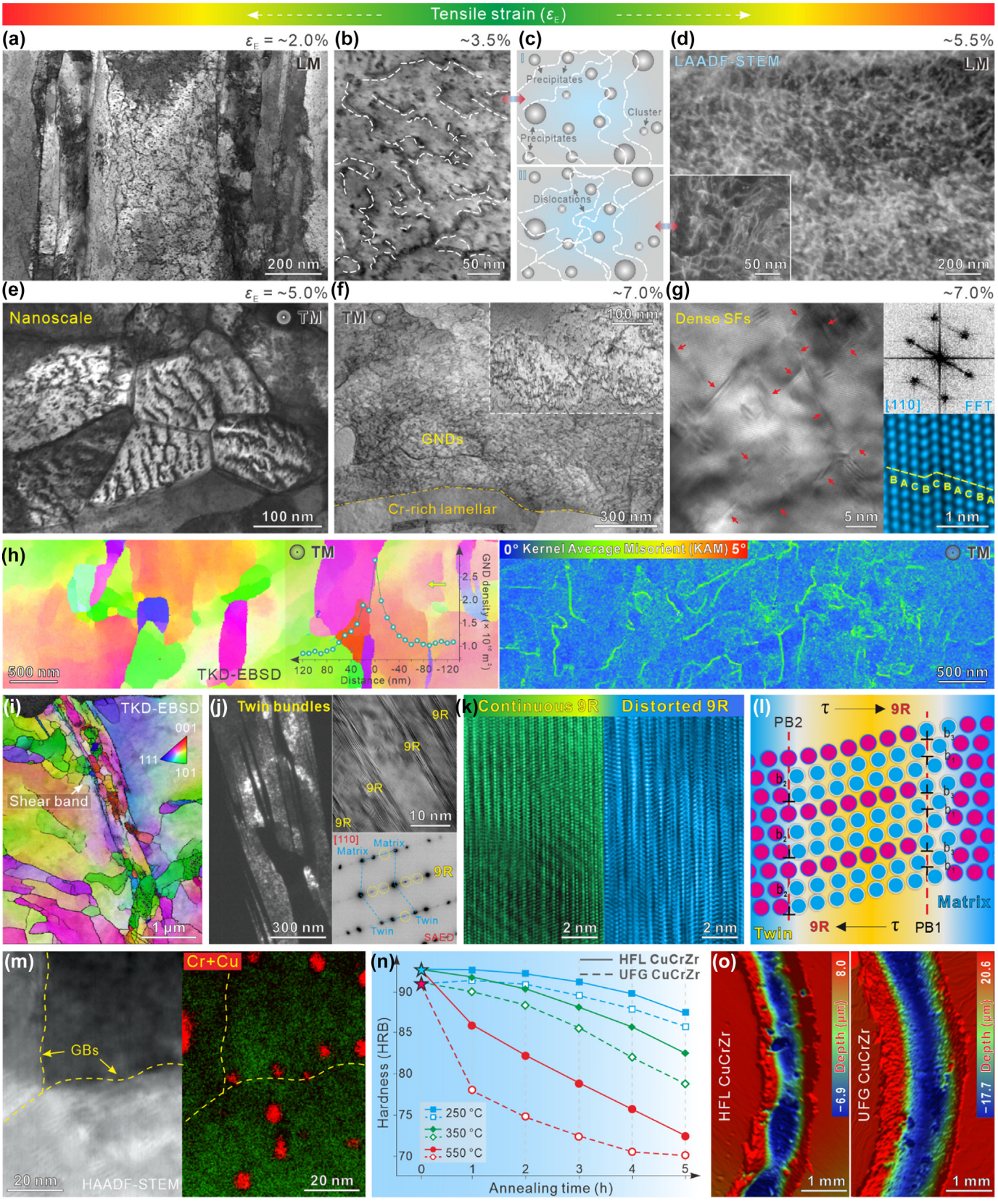
Tensile strain (ε_E)
(a)
ε_E = ~2.0%
LM
200 nm
(b)
~3.5%
50 nm
(c)
I
Precipitates
Cluster
Precipitates
II
Dislocations
(d)
~5.5%
LAADF-STEM
LM
50 nm
200 nm
(e)
ε_E = ~5.0%
Nanoscale
TM
100 nm
(f)
~7.0%
TM
100 nm
GNDs
Cr-rich lamellar
300 nm
(g)
~7.0%
Dense SFs
5 nm
[110]
FFT
B A C B C B A C B A
1 nm
(h)
TM
500 nm
TKD-EBSD
GND density (× 10^{15} m^{-2})
2.5
2.0
1.5
1.0
120 80 40 0 -40 -80 -120
Distance (nm)
0° Kernel Average Misorient (KAM) 5°
TM
500 nm
(i)
TKD-EBSD
001
111
101
Shear band
1 μm
(j)
Twin bundles
300 nm
9R
9R
9R
9R
10 nm
[110]
Matrix
Matrix
9R
Twin
Twin
SAED
(k)
Continuous 9R
Distorted 9R
2 nm
2 nm
(l)
τ
9R
PB2
Matrix
Twin
9R
τ
PB1
(m)
Cr+Cu
GBs
20 nm
HAADF-STEM
20 nm
(n)
HFL CuCrZr
UFG CuCrZr
Hardness (HRB)
90
85
80
75
70
250 °C
350 °C
550 °C
0 1 2 3 4 5
Annealing time (h)
(o)
HFL CuCrZr
8.0
Depth (μm)
-6.9
1 mm
UFG CuCrZr
20.6
Depth (μm)
-17.7
1 mm

The evolution of deformation substructures was also characterized through multiple TEM imaging at the nanoscale to reveal the underlying mechanisms responsible for the high ductility. At a low strain, larger subgrains (>300 nm) preferentially deformed within the low-strength coarse-grained lamellae (>1 μm) (Fig. 5a). Moreover, excellent strain compatibility was detected between subgrains due to the intrinsically high dislocation transmissibility at LAGBs [39], effectively homogenizing the intragranular plastic deformation (Supplementary Fig. 11).

With increasing tensile strains, the gliding dislocations interact intensively and frequently with nanoprecipitates thanks to their high number density. It is often observed that an individual dislocation line becomes very wavy, manifesting as partly forward and partly backward in an alternate pattern, even within a range of less than 100 nm (Fig. 5b). This phenomenon prevails because the gliding dislocation lines encounter dense bimodal precipitates and potential solute clusters. The obstacles exert varied pinning forces on dislocation movement that cause the observed various twisted dislocation shapes (Fig. 5b, d). These varying interaction processes consequently motivate significant dislocation proliferation (Fig. 5d). Furthermore, in the dynamics of this process, massive dislocation lines sweeping through the dense heterogeneous field of nanoprecipitates slow down, and their forward progression has to proceed via local segments cutting through and de-trapping from the precipitates. The induced "sluggish" process, due to numerous local "pinning-and-depinning" incidents, thus maximizes the opportunities for dislocations to interact with each other, favouring dislocation entanglement and further dislocation accumulation, as schematically illustrated in Fig. 5c. No excessive dislocation pile-ups are found around nano-precipitates, suggesting that the low-misfit coherent matrix/precipitate interfaces can minimize the elastic strain accumulation resulting from dislocation shear and hence prevent crack initiation at these interfaces [40]. Eventually, these dynamic, topologically varied interactions promote extensive forest-dislocation hardening and high uniform elongation [41].

With the progressive hardening of large micron-grains, critical deformation stresses are gradually reached in neighbouring submicron lamellar grains. It was observed that the smaller grains also initiate plastic deformation, accompanied by appreciable dislocation accumulation, which was even detected in the nanograins of ~100 nm (Fig. 5e). Thus, an alternative hardening source afforded by the tiny grains is sequentially activated and supplemented to our HFL material. Moreover, through synchronous high-energy X-ray diffraction (HE-XRD) probing at this hetero-deformation stage, we found an ultrahigh dislocation density up to $\sim 3.2 \times 10^{15}\,m^{-2}$ (Fig. 4b), which is rarely observed before in CuCrZr materials subjected to room-temperature tensile deformation. The unusual trend further supports our microstructural finding (Fig. 5a–e) that it is the efficient dislocation accumulation that substantially contributes to sustaining effective strain hardening (Fig. 4b).

To better track the compatible intergranular hetero-deformation, the on-axial, high-precision TKD-EBSD characterizations were implemented (Fig. 5h). A gradual increase in the kernel average misorientation (KAM) is clearly detected around multimodal grain boundaries, indicative of a gradient accumulation of geometrically necessary dislocations (GNDs). The GND gradients allow denser dislocation accumulation (inset, Fig. 5h) and promote the HE-XRD-identified exceptionally high dislocation density. Moreover, the GND gradients can effectively coordinate the intergranular hetero-deformation and produce back stress in the opposite direction of the applied shear stress [42]. Meanwhile, the developed back stress will exert a forward stress on the adjacent hard zone, which, for instance, have enabled significant plastic deformation in the nanograins in Fig. 5e. Hence, strong hetero-deformation-induced (HDI) hardening is expected due to the kinematic interplay between two kinds of stresses around hetero-zones [42]. Further high-magnification STEM probing also identifies the gradient GNDs, which are more intense in the Cr-lamellar vicinity (Fig. 5f). The intensified trend arises from the poor plastic deformability of Cr lamellae, which requires more prominent GND operations to relieve stress concentrations and sustain intergranular hetero-deformation. Therefore, more intensive back stress is developed, high enough to activate abundant stacking faults (SFs) and SF-mediated Lomer–Cottrell locks (Fig. 5g). As an appended deformation mode, the stress-activated SFs, together with their dynamic interactions with precipitates and dislocations, can further alleviate stress concentrations around the Cr lamellae and allow for additional strain hardening.

Our results have revealed that the distinctive HFL design can consecutively activate the next hardening mechanisms (e.g., HDI hardening) in sequence when an early (precipitation) hardening capacity is gradually exhausted, thereby enabling excellent strain-delocalization ability shown in Fig. 4h. To gain deeper insight into the sequentially-activated phenomena, the loading–unloading–reloading (LUR) experiment was further performed (Supplementary Fig. 12). At the early strain stage (0.5~4.0%), we detect high effective stress, which is ~1.3 times

FIG. 5

Multiscale dynamic deformation interactions and hardening mechanisms. a, **b,** Two STEM images. **c,** Corresponding schematic diagrams revealing intensive interactions among dislocations and nanoprecipitates in (**b**) as well as dislocations and precipitates or dislocations in (**d**). **d,** Low-angle ADF (LAADF)-STEM image and its inset revealing extensive dislocation tangle and proliferation. **e,** TEM image. **f,** STEM image and STEM inset showing dense GND pile up. **g,** High-resolution TEM image as well as fast Fourier transform (FFT) and atomic-resolution TEM insets revealing dense SFs and SF-mediated Lomer-Cottrell locks. **h,** TKD-EBSD IPF and corresponding KAM images. **i,** TKD-EBSD IPF image showing SBs. **j,** TEM images and selected area electron diffraction (SAED) pattern revealing twins and the 9R phase. **k,** Atomic-scale TEM image of continuous and distorted 9R phases. **L,** Atomic schematic diagram of the 9R-mediated twining. **m,** HAADF-STEM image and STEM-EELS mapping revealing that the Cr-rich precipitates can significantly pin grain-boundary movement and elevate the thermal stability of materials. GBs refer to grain boundaries. **n,** Rockwell hardness evolution with annealing time (1~5 h) at annealing temperatures of 250 °C, 350 °C and 550 °C in the UFG and HFL samples. **o,** Confocal laser scanning microscopy observations of the 3D friction and wear morphology in UFG and HFL samples. In terms of lower wear width and depth, our HFL material thus displays significantly better wear resistance than the ECAP UFG counterpart.

the HDI stress (Fig. 4f). This finding agrees with our microstructural observations (Fig. 5a–d) that due to atomic-scale coherent features, nanoprecipitates allow shearing and traversal of dislocations to mediate plastic deformation at low strains. The ensuing high frequency and density of local short-range interactions thus contribute to substantial effective stress [40]. Although the HDI stress is initially lower, it, however, shows a steep increase and nearly approaches the effective-stress level at the later strain stage (Fig. 4f). This change can closely correlate with those detected long-range, gradient GNDs (Fig. 5f, h), which elevate the HDI stress due to the induced kinematic interaction between the back and forward stresses [42]. Taken together, the LUR-related results quantitatively corroborate our multiscale microstructural observations and enhance our understanding for the bioinspired, sequentially-activated strain hardening behaviour.

When the topologically-varied intra/intergranular hardening mechanisms are exhausted progressively and consecutively, local plastic deformation initiates, as demonstrated by prior DIC observations (Fig. 4i). Yet the local deformation is governed by dense and stable shear bands (SBs), manifesting as a multiple interlocking state (see OM and SEM images; Fig. 4i). This scenario contrasts sharply with the usual catastrophic propagation and damage of single macroscopic SBs (once initiated), as observed in our and those reported high-strength CuCrZr materials [29–39] (inset, Fig. 4a). By applying correlative SEM-focused ion beam (FIB) techniques, the site-specific sampling for SBs was carried out to investigate their substructural response (Supplementary Fig. 13). Coupled TKD-EBSD and TEM characterizations reveal a nanostructured SB composed of certain elongated nano/ultrafine grains (produced by shearing deformation) and profuse stress-activated nano-twinning bundles (Fig. 5i, j). Further high-resolution TEM imaging detects many distinctive 9R phases with various distortion degrees, especially at the front end of nanotwins (Fig. 5j, k). The stress-activated twinning, as illustrated in Fig. 5l, was developed through the migration of these 9R phase-mediated $\sum 3\{1\,1\,2\}$ incoherent twin boundaries (Supplementary Note 6) [42–44].

The 9R-mediated twinning is rarely detected in materials with medium-to-high stacking fault energies (SFEs), which requires sufficiently high critical stresses and/or strain rates [44–46]. For example, Xue et al. [43] obtained the 9R-phase component of tens of nanometres in high-SFE pure Al by using a laser-induced projectile impact (with extreme shock stress and speed). Hence, the shearing deformation induced by SBs is deduced to activate local ultrahigh internal stresses that trigger the unusual twinning. More importantly, strong strain hardening is developed due to dynamic substructure refinement induced by twinning and the 9R phase as well as their intensive deformation interactions with lattice dislocations and nanoprecipitates (Supplementary Fig. 14). These hardening processes, operating at the front end of SBs, substantially buffer and hinder their destructive growth. The resulting constraint on the activated SBs enables other SBs to form at some adjacent locations, thereby inducing stable multiplication and an interlocking network of SBs (Supplementary Fig. 15). Despite operating within local zones, these SBs, characterized by a self-hardening ability, hence stabilize the necking deformation, leading to the extremely weak stress drop (Fig. 4a). Furthermore, through *in-situ* HE-XRD experiments, it was further unveiled that the coupled deformation modes of SFs, nano-twinning and 9R phase effectively suppress recovery and promote accumulation of dislocations (Supplementary Note 7). The resulting sustained high dislocation density revealed in Fig. 4b quantitatively rationalizes the observed weak stress reduction during the necking stage, thus affording additional tensile ductility.

Overall, independent of the modification for compositions and phase constituents, our bioinspired, heredity-derived hierarchical design has activated many previously unattainable deformation and hardening mechanisms (Fig. 5a–l), due to the HFL-induced diverse complex internal stresses. These scenarios are quite unexpected, yet absolutely essential, in light of the present exceptional strength–ductility enhancement (Fig. 4a).

Our HFL-reinforced material also exhibits an ultrahigh electrical conductivity of 79.6% IACS. The resulting strength–ductility–conductivity combination surpasses that of all other CuCrZr alloys and their massive alike or derived material systems reported to date (Fig. 4d). Meanwhile, the record-high strength–ductility–conductivity combination (irrespective of other salient fabrication and performance advantages) in our HFL-reinforced material is also highly competitive with those of other classes of state-of-the-art bulk copper alloys (see details in Supplementary Fig. 16, Supplementary Table 1). Here, our high conductivity primarily results from dense Cr and Zr coprecipitates/clusters and interfacial Zr segregation (Fig. 2), which, together with relatively low initial dislocation density, result in a high-purity Cu matrix (Fig. 3b) [18–22]. This purification can reduce lattice distortion and weaken the scattering degree for conductive electrons, thereby enabling high conductivity [18–22]. Second, the HFL material has a low proportion of transverse grain boundaries (~26%) and considerable high-coherence LAGBs (instead of atomically disordered HAGBs) (Fig. 1d–h). This coupled boundary trait can remove and/or weaken boundary barriers to the electronic transmission, favouring high conductivity [18–22]. Hence, benefiting from all-relevant-length scales, this boundary engineering operating from the micron to nanoscale, in conjunction with purifying the Cu matrix at the atomic scale, resembles the multiscale functioning adaptation found in bamboo and other plant trunks. To maximize the nutrient supply, for instance, their organizational structures generally evolve one-way, barrier-free hierarchical transport channels [9].

In actual service, the CuCrZr materials simultaneously need to be critically equipped with excellent thermal stability. Therefore, the hardness change of our HFL material was measured at different annealing temperatures and holding times, as well as that of the UFG ECAP material for comparison (see Fig. 5n). At relatively low temperatures of <400 °C, both samples could maintain a hardness decrease of less than 16% within 5 h. However, at a higher temperature (550 °C), the hardness of the UFG counterpart significantly decreased by >16% in only 1 h, while our HFL material exhibited salient thermal stability, in which the hardness decreased by only 15% within 3 h. Here, decent low-temperature thermal stability in the UFG counterpart can be ascribed to the dispersed intergranular precipitates (inset, Fig. 1c), which can pin boundary movement and inhibit grain coarsening. Such structural characteristics and thermostability

mechanisms were also reported in other high-strength UFG CuCrZr alloys, thus exhibiting similar trends of thermal stability [18–22]. At elevated temperatures, the large thermostability difference can be attributed to several tailored factors, which are not available to those UFG counterparts, but collectively play in our HFL material. First, the Zr segregation (Fig. 2e–h) can reduce the HAGB energy, while numerous LAGBs (Fig. 1f) intrinsically feature a low energy state. These factors, taken together, elevate the coarsening resistance of grains [24]. Second, precipitates can pin boundary movement (see Fig. 5m) and suppress coarsening, especially for the present dense, coherent nanoprecipitates (Fig. 1j–l), which are expected to be more stable at 550 °C, and thus, are more efficient than the larger intergranular precipitates in the UFG counterpart [46,47].

In terms of the tolerance to ultrahigh-speed deformation, our HFL material exhibits enhanced dynamic tensile properties and salient impact toughness. This property trait/superiority can guarantee a large safety margin before fracture when applied under extreme loading environments. Compared to the quasi-static tensile loading ($\sim 1 \times 10^{-3}$ s^{-1}), ultrahigh strain rate ($\sim 1 \times 10^{2}$ s^{-1}) with higher internal stress activated the 9R-phase-assisted twins in advance. They occur during the uniform-deformation stage rather than after (Supplementary Fig. 17). Afterwards, denser SB activities are detected (Supplementary Fig. 18). These intensified mechanisms collectively enable markedly better dynamic strength–ductility combination (Fig. 4g, Supplementary Fig. 19). Additionally, our HFL material–resembling the hierarchical lamellar-structured biomaterials [48–50], as exemplified by bone and nacre–enables multiple intrinsic and extrinsic toughening mechanisms interacting under varying internal stress states and length scales (Supplementary Figs. 20, 21 and Supplementary Note 8). The complementary mechanisms, therefore, boost superior impact energy of 16.08 ± 0.38 J, over twice that of the UFG counterpart (inset, Fig. 4g). These appreciable dynamic properties combined with high thermal stability, to some extent, also rationalize the observed excellent friction and wear resistance (Fig. 5o, Supplementary Figs. 22, 23). Thus, additional excellent property paradigms can also be expected, e.g., the fatigue behaviour, especially when considering our HFL material with the precipitation-free zone (PFZ)-decorated substructural trait (Fig. 2a). Recent studies have shown that PFZs can be intentionally tailored to enhance fatigue life of the precipitation-hardened alloy systems [51]. Moreover, our designed HFL structure features excellent casting-flaw tolerance (Supplementary Fig. 24). Hard and brittle inclusions, for instance, are inevitably introduced in actual industrial production. They often cause severe stress concentrations during external loading, leading to cracking and quick failure of workpieces. This creates enormous risk for engineering structures, as well as for human lives. However, such fatal events can be effectively deterred by our bioinspired, heredity-derived HFL design (Supplementary Fig. 24).

Concluding remarks

In conventional processing, to homogenize compositions and microstructures to eliminate the potential adverse impacts of dendrites, the as-cast bulk materials, before severe plastic processing, are usually subjected to costly high-temperature and lengthy homogenization treatments (Supplementary Table 2) that have a large negative environmental footprint. Here, these dendritic structures are counterintuitively exploited via optimized processing routes rather than avoiding them. This economic processing route provides essential prerequisite to the bionic structural-hierarchy design. The built HFL structure concomitant with complex varied internal stress states activates many distinct but critical reinforcement mechanisms and biomimetic attributes that collectively circumvent multiple property trade-offs.

Moreover, the tailored Cu-1.0wt%Cr-0.1wt%Zr HFL material with the same micro-alloyed composition and simple phase constituents as the traditional homogeneous-structured CuCrZr counterparts, yet, exhibits far better multifunctional properties, as quantitatively exemplified in Fig. 4e. Again, this is reminiscent of versatile natural materials, of which wisdom resides in activating all-length-scale functional adaptations by constructing exquisite hierarchical architectures, despite a very limited component supply as well as choice.

In summary, we have successfully conceived and demonstrated an effective bioinspired, heredity-derived engineering strategy, elucidated the underlying process–structure–multifunction relationship, and achieved the desired-yet-challenging paradigm from the bionic multiscale design to high figure-of-merit bulk multifunctionality. Both the multifunctional properties and attributes are unprecedented as well as of great commercial and technological importance, making our HFL materials broadly promising in railway contact wires and networks, new energy electric vehicles, electric/microelectronic connectors, integrated circuit lead frames, resistance welding electrodes and heat exchangers in fusion reactors. Compatible with current high-efficient and cost-effective industrial practices, it is anticipated that our bioinspired, heredity-derived strategy will find more crucial applications in other alloy systems, thereby delivering a conceptual change in the design of high-performance, next-generation structural and functional integrated bulk materials.

Materials and methods

Specimen preparation

The studied alloy with a nominal composition of Cu-1.0wt%Cr-0.1wt%Zr was produced by industrial continuous casting. The as-cast CuCrZr bar prepared with ~30 mm in diameter was continuously extruded to ~20 mm, and then dwindled to the application-oriented ~14 mm after multi-pass rotary swaging. The as-processed samples were subsequently aged at 450 °C for 3 h in a muffle furnace, followed by water quenching. Another as-cast CuCrZr bar, prior to ECAP, was homogenized in an air circulated furnace at 1000 °C for 5 h followed by water quenching. ECAP was performed with 0.4 mm/s velocity at room temperature via the so-called "route Bc" in a 90°die, which leads to an imposed strain of about 1.0 per pass. The ECAP process was carried out for 8 passes, after which the grains cannot be further refined and the mechanical property would not be further improved. The ECAP-processed samples were subsequently aged

at 460 °C for 2 h in a muffle furnace followed by water quenching.

OM, SEM and EBSD observations

Optical microscopy (OM) characterization was performed on a Zeiss Axio Imager Z2m. Electron back-scattering diffraction (EBSD) and scanning electron microscopy (SEM) observations were conducted on a Zeiss Gemini 300 scanning electron microscope (SEM) equipped with an Oxford EBSD system. EBSD specimens were initially polished with the 2,000-grit SiC paper and subsequently electrochemically polished using a 25% nitric acid solution (volume percent, vol.%) at a direct voltage of 30 V at room temperature.

Multiple, multiscale TEM observations and atomic-resolution STEM-EELS mapping

Transmission electron microscopy (TEM) and high-angle annular dark-field scanning TEM (HAADF-STEM) analyses were conducted on JEOL JEM-2010 and JEM-2100 at 200 kV. For low-angle annular dark-field (LAADF) imaging, a probe semi-convergence angle of 17 mrad and inner and outer semi-collection angles from 14 mrad to 63 mrad were utilized. Ultrahigh-resolution STEM investigations were carried out by using a spherical aberration-corrected STEM (JEM-ARM200F, JEOL Co. Ltd.) equipped with a cold-field emission gun and a DCOR probe Cs-corrector (CEOS GmbH) operated at 200 kV. The HAADF-STEM images were obtained by an ADF detector with a convergent semi-angle of 20.4 mrad and collection semi-angles of 70–300 mrad. For LAADF-STEM imaging, the convergent semi-angle and collection semi-angles are 20.4 mrad and 28–72 mrad, respectively. To improve the signal-to-noise ratio (SNR) and to minimize the drift and the image distortion of high-angle annular dark-field (HAADF) images, 8 serial frames were acquired with a short dwell time (2 μs pixel^{-1}). The image series were then aligned and superimposed. A collection semi-angle of 111 mrad was used for EELS measurements with a Gatan GIF Quantum ERS electron energy-loss spectrometer equipped with K2 Summit camera. EELS spectrum imaging was performed with a dispersion of 0.5 eV/channel and 900 eV drift tube energy with a 4000-pixel wide detector for the simultaneous acquisition of Cu-L (931 ev) and Zr-L (2222 eV) spectrum images. The raw spectrum image data were denoised by applying a principal component analysis (PCA) with a built-in multivariate statistical analysis (MSA) plugin in Gatan Digital Micrograph. TEM specimens were first mechanically ground to ~30 μm thickness and then twin-jet electropolished using a 30% (vol.%) nitric/methanol acid solution at –30 °C. Some high-quality TEM specimens are fabricated particularly through focused ion beam (FIB) sampling.

FIB site-specific sampling

Some TEM specimens for site-specific shear-band observations through high-precision, on-axial TKD-EBSD and multiple TEM examinations were prepared with FEI HONGKONG 600i dual-beam FIB in multiple steps starting with 30 kV Ga+ ions down to 5 kV ions for reducing surface damage induced by the high energy ions. The sample was tilted 52 ± 1.1°, and the Ga ions strike perpendicular to the sample surface. For the obtained elementary TEM sample, the angles of Ga ions striking the sample will be lowered to ± 2°, so as to access the uniform sample thinning.

High-precision, on-axis Transmission Kikuchi Diffraction (TKD) EBSD

The on-axis TKD investigation of samples was performed on a Bruker Optimus TKD detector operated at an acceleration voltage of 30 kV. The FIB-TEM sample was mounted with the TKD head positioned immediately beneath the sample. TKD orientation maps were acquired over a large number of particles with a scan step of 12 nm and exposure time of approximately 6 ms per point with a pattern resolution of 898 × 674 pixels.

3D Atom probe tomography

The near-atomic scale elemental information of the as-processed CuCrZr was gathered using a LEAP™ 5000X HR (CAMECA) under a high vacuum of 2×10^{-11} Torr. Atom probe tomography (APT) experiment was run in the laser mode with a specimen temperature of 60 K, a pulse rate of 125 kHz, laser energy of 40 pJ, and a detection rate of 0.5%. The APT results were reconstructed and analyzed employing the CAMECA integrated visualization and analysis software (IVAS 3.8.6). Needle-shaped samples for APT characterizations were prepared using a site-specific FIB lift-out procedure, sharpened using a 30 kV Ga+ ion beam, and cleaned using a 2 kV ion beam.

Quasi-static tension

Dogbone-shaped tensile samples with a cross section of 3.2 × 0.8 mm^2 and a gauge length of 13 mm were cut from two types of processed samples by wire electro-discharge machining. For the bioinspired HFL sample, the corresponding tensile samples were cut parallel to the longitudinal section. Room-temperature tensile and LUR tests were conducted in an MTS Criterion Model 44 machine with an initial strain rate of $\sim 1 \times 10^{-3}$ s^{-1}. Before testing, these sides of the gauge section were carefully ground to a 2500-grit finish using SiC grinding papers. To obtain a reproducible tensile state, all tensile tests were repeated five times at least. All tensile tests were conducted, using a 10-mm extensometer to monitor the strain.

Loading–unloading–reloading (LUR) testing

The condition for LUR tests was the same as that of the monotonic tensile test. Upon straining to a designated strain at the strain rate of $\sim 1 \times 10^{-3}$ s^{-1}, the specimen was unloaded in load mode to 20 N at the unloading rate of 200 N min^{-1}, followed by reloading at a strain rate of $\sim 1 \times 10^{-3}$ s^{-1} to the same applied stress before the next unloading. According to the method reported in Refs. [27,28], the flow stress was divided into the back stress and the HDI stress.

In-situ tensile test with SEM observation and digital image correlation (DIC) analysis

In-situ SEM tensile test was conducted on a loading stage from Zhejiang Qiyue Mechanical Technology consisting of a 2 kN load cell. The stage is set up inside a Zeiss Gemini 300 SEM chamber. The sample was tested at a strain rate of $\sim 1 \times 10^{-3}$ s^{-1}. Before the test, mechanically polishing and chemically etching were per-

formed in order to acquire high-quality microstructural images. During tests, both force–displacement data and video imaging were synchronized for the desired one-to-one structure–property relationship.

Tensile tests with DIC analysis were carried out using the same condition as monotonic quasi-static tension and ultrahigh-speed tensile testing. The front surface of tensile samples was sprayed with white and black paint by airbrush to make speckles for DIC analysis. Images of the sample surface were collected, at fixed time intervals, using a high-speed CCD camera which aligned normal to the specimen surface. In all the tests, the surface was illuminated by two halogen lamps mounted at either side of the camera. The digital images obtained were processed using VIC-2D software to produce a displacement field, strain field, and strain rate field. Similarly, the lamellar structure of the CuCrZr sample during SEM observation can also be used for DIC analysis.

Ultrahigh-speed tensile testing

High strain-rate tensile tests at room temperature in the air were conducted using an Instron (VHS 160/100-20) testing machine, and its maximum loading speed is 20 m/s and maximum dynamic load is 100 kN. During dynamic tensile tests, the piezoelectric sensor of the testing machine was used to gather dynamic tensile load, and the high-speed camera system combined with the non-contact test analysis software was applied to test dynamic tensile strain. Dynamic tensile specimens had a gauge length of 12.5 mm with a cross section of 4 mm × 0.65 mm^2, and the high strain rate is ~1 × 10^2 s^{-1} in the present work. The other condition for dynamic tensile tests was the same as that of those quasi-static ones.

Impact toughness testing

To evaluate the impact toughness properties, Charpy impact tests were conducted on sub-size Charpy 45° V-notch specimens with a size of 5 × 5 × 55 mm^3 [in accordance with ASTM Standard E23 [54]. The depth of the notch and the diameter at the base of the notch are ~1 mm and ~0.25 mm, respectively. For the bioinspired HFL sample, the corresponding Charpy impact samples were cut parallel to the longitudinal section. The impact experiment was conducted by a 150-J-capacility MTS impact testing machine. At least three samples were tested to ensure repeatability for these two types of processed CuCrZr samples.

Hardness and conductivity measurements

Rockwell hardness was measured at room temperature using a fully-automatic Rockwell diamond indenter (Wilson WH2002T) equipped with a 1.588 mm diameter steel ball at 100 kgf load. The distance between the centers of two adjacent indentations was controlled to be at least three times the diameter of the indentation (in accordance with ASTM standard E18-22). The electrical conductivity was measured by a Fischer SMP350 conductivity meter at room temperature (20 °C), using specimens with a cross-section of 15 mm × 15 mm and a thickness of 20 mm.

Tribological, weight loss and 3D surface topography testing

CuCrZr alloy disk and GCr15 ball counterparts were used for ball-on-disk wear tests. Before the wear test, the surface of the specimen disk was ground and polished to 0.1 μm. The wear tests were performed under a 15 N normal load and at a sliding speed of 0.1 m s^{-1} for 20 min corresponding to a sliding distance of 120 m. 3D surface topography of the wear track was investigated by an optical microscope (Bruker, Contour GT-K and Carl-Zeiss, Germany). Weight loss values of all processed specimens were measured by an electronic balance (Precisa, FA1204C) with a precision of ± 0.1 mg. The wear rate value was calculated using the weight loss of the specimen. Worn surfaces of the tested specimens were analyzed using a confocal laser scanning microscopy and an SEM (TESCAN, VEGA 3 Easy Probe) for all testing conditions so as to determine the operative wear mechanisms.

Synchrotron-based high energy X-ray diffraction

In-situ high-energy X-ray diffraction measurements were carried out on the beam-line 11-ID-C, at the Advanced Photon Source, Argonne National Laboratory (APS, ANL), USA. The experimental set-up was described in full detail in Ref. [2]. Dimensions of the tensile specimen in the gage part were 10 mm (length) × 3 mm (width) × 0.8 mm (thickness). During tensile loading, a monochromatic X-ray beam with energy ~105 keV (λ = 0.1173 Å) and beam size of 500 μm (height) × 500 μm (width) was used. A 2-D detector was placed ~1.7 m behind the tensile sample to record the scattering intensity. Crystallographic planes were determined from the diffraction patterns, and the lattice strains were calculated from the change of the measured inter-planar spacing.

The modified William–Hall (WH) method was used to calculate the dislocation density from the synchrotron X-ray diffraction profiles [25,55]. In the WH method, the broadening of the diffraction peaks was assumed to be related to the average crystalline size (D) and dislocation density (ρ) as [25,55]:

$$\Delta K \cong \frac{0.9}{D} + \left(\frac{\pi A^2 B^2}{2}\right)^{\frac{1}{2}} \rho^{\frac{1}{2}} (KC^{\frac{1}{2}}) \quad (1)$$

ρ can be estimated using the slope (m) of the fitted curves on the ΔK *vs* $KC^{\frac{1}{2}}$.

The detailed parameters are based on the following equations and tables:

$$K = \frac{2\sin\theta}{\lambda} \quad (2)$$

$$\Delta K = \frac{2cos\theta(\Delta 2\theta)}{\lambda} \quad (3)$$

θ	Bragg position	Get from data
Δθ	Full-width at half-maximum (FWHM) of the diffraction peak at θ	Get from data
A	A constant determined by the effective outer cut-off radius of dislocations	2 [25,55]
b	Magnitude of the Burgers vector	0.2556 nm [18,21,22,29]
C	Average dislocation contrast factor for each {*h k l*} reflection	$C = C_{H00}\left\{1 - q\left[\frac{h^2k^2+k^2l^2+h^2l^2}{(h^2+k^2+l^2)^2}\right]\right\}$

Here, C_{H00} and q are constants related to the anisotropic elastic constants (C_{11}, C_{12} and C_{44}) as [55]:

$$C_{H00} = a\left[1 - \exp\left(-\frac{A_i}{b}\right)\right] + cA_i + d \quad (4)$$

$$q = a\left[1 - \exp\left(-\frac{A_i}{b}\right)\right] + cA_i + d \quad (5)$$

$$A_i = \frac{2C_{44}}{C_{11} - C_{12}} \quad (6)$$

DDD simulation

3D discrete dislocation dynamics (DDD) simulations were performed to quantify the coherency strengthening using an in-house modified version of Parallel Dislocation Simulator (ParaDiS), originally developed at Lawrence Livermore National Laboratory [56,57]. 3D DDD is a mesoscale approach that directly simulates the collective dynamic behaviors of dislocations [58,59]. In our DDD simulations, with the existence of precipitates, dislocations are subject to an additional coherency stress term, which is induced by the lattice misfit between precipitates and matrix [60]. Based on the experimental measurements, there are two types of Cr-rich precipitations in the Cu matrix. Type 1 corresponds to the nanoscale (3∼6 nm) precipitated particles formed during aging, and type 2 to the particles with a size range of 10∼14 nm, formed in the extrusion process and ageing. The type 1 precipitates constitute a larger precipitate density (defined as the number of precipitates per unit volume) of 1.42×10^{23} m^{-3} and have a lattice misfit of $\varepsilon_{p1} = 0.334\%$, while the coarser type 2 precipitates are sparsely distributed with a lower density (6.95×10^{20} m^{-3}) and a misfitting strain of ε_{p2} =0.550%. For randomly generated spherical precipitates with the measured particle sizes, precipitate densities and misfitting strains, the induced coherency stress field can be calculated based on the Eshelby inclusion model [61–63], and will be fed into DDD simulations.

In this work, a series of DDD simulations in pure Cu were performed in a 1 μm × 1 μm × 1 μm simulation volume with different initial dislocation and precipitate microstructures, subject to uniaxial tensile loadings at the constant strain rate of 200 s^{-1} along the [0 0 1] crystallographic orientation, under the periodic boundary conditions.

MD simulation

Large scale molecuar dynamics (MD) simulations were performed to quantitatively investigate the hardening effects of Cu-Cr nanoprecipitates using the open-source code LAMMPS [64]. Dislocation structure analysis was performed and visualized using OVITO [65]. Coherent Cu-Cr nanoprecipitates with a diameter of 5 nm were randomly introduced into 20 nm × 20 nm × 20 nm copper matrix according to the experimentally measured density of 1.42×10^{23} m^{-3} by replacing 25 % of Cu atoms with Cr atoms inside the precipitates. The atomic interaction between Cu and Cr atoms were described by the recently developed embedded atom method (EAM) potential [66]. Periodic boundary conditions were adopted in all three directions. The initial dislocation structures were generated by randomly introducing dislocation loops into the pristine sample, followed by relaxation under external stresses and zero stresses sequentially [67]. The relaxed samples were subsequently deformed along the [0 0 1] crystallographic orientation at a constant strain rate of 5×10^8 s^{-1}. The isothermal–isobaric (NPT) ensemble was used for all simulations during the tensile loading with temperature kept at 300 K and zero pressure in non-deforming directions.

Author contributions

P.J.S. designed the study, and carried out the main experiments. Y.T.Z., H.J.G., C.T.L., Y.B.Z., Y.R., W.L.R., Z.S.L. Z.S. and P.J.S. analysed the data and wrote the main draft of the paper. H.G. W. and P.A.v.A. conducted STEM&EELS measurements and related data analysis. N.M., J.C.P., Y.T.Z., C.Y.L. and P.J.S conducted multiple TEM characterizations. Y.L. and N.N.L. conducted site-specific FIB sampling and EBSD characterizations. Y. R. and J.Y. conducted the high-energy synchrotron XRD. J.H.L. conducted 3D-APT characterizations. Z.L. and Y.J.G. conducted 3D DDD and MD simulations. Y.L., Z.Z.L, M.Y.W., Y.P.Y., B.D., T.S.L., Z.S. and P.J.S. processed various experimental samples. All authors contributed to the discussion of the results, and commented on the manuscript.

Data availability

Data will be made available on request.

Declaration of Competing Interest

The authors declare that they have no known competing financial interests or personal relationships that could have appeared to influence the work reported in this paper.

Acknowledgements

Y.T.Z. is grateful for financial support from National Key R&D Program of China (2021YFA1200202) and national Natural Science Foundation of China (No. 51931003). Y.B.Z. is grateful for financial support from National Key R&D Program of China (2018YFB0109404, 2022YFC2904901, 2022YFC2904903 & 2022YFC2904905). C.T.L. is also grateful for the financial support from the Hong Kong Institute for Advanced Study (grant no. 9360157). Z.S. is grateful for financial support from National Natural Science Foundation of China (No. 51904184 and 52274385). B.D. is grateful for financial support from National Natural Science Foundation of China (No. 52204392). The authors from City University of Hong Kong (CityU) are grateful for the internal funding from CityU under the programs 9042635, 9360161, and 9380060. This project has received funding from the European Union's Horizon 2020 research and innovation program under Grant Agreement No. 823717–ESTEEM3. Use of the Advanced Photon Source was supported by the U.S. Department of Energy, Office of Science, Office of Basic Energy Science, under Contract No. DE-AC02-06CH11357.

Peijian Shi designed the study, and carried out the main experiments.

Yuntian Zhu, Huajian Gao, C.T. Liu, Yunbo Zhong, Yang Ren, Weili Ren, Zuosheng Lei, Zhe Shen and Peijian Shi analysed the data and wrote the main draft of the paper.

Hongguang Wang and Peter A. van Aken conducted STEM&EELS measurements and related data analysis.

Na Min, Jianchao Peng, Yangtao Zhou, Chunyan Ling and Peijian Shi conducted multiple TEM characterizations.

Yi Liu and Ningning Liang conducted site-specific FIB sampling and EBSD characterizations.

Yang Ren and Jie Yan conducted the high-energy synchrotron XRD. **Junhua Luan** conducted 3D-APT characterizations.

Zhi Li and Yejun Gu conducted 3D DDD and MD simulations.

Yi Li, Zhongze Lin, Mingyang Wang, Yinpan Yang, Biao Ding, Tengshi Liu, Zhe Shen and Peijian Shi processed various experimental samples. All authors contributed to the discussion of the results, and commented on the manuscript.

Appendix A. Supplementary material

Supplementary material to this article can be found online at https://doi.org/10.1016/j.mattod.2023.11.003.

References

[1] L. Lu et al., Science 304 (2004) 422–426, https://doi.org/10.1126/science.1092905.

[2] P.J. Shi et al., Science 373 (2021) 912–918, https://doi.org/10.1126/science.abf6986.

[3] L.L. Han et al., Nature 608 (2022) 310–316, https://doi.org/10.1038/s41586-022-04935-3.

[4] Q.Z. Mao et al., Nano Lett. 21 (2021) 3191–3197, https://doi.org/10.1021/acs.nanolett.1c00451.

[5] H.J. Gao et al., PNAS 100 (2003) 5597–5600, https://doi.org/10.1073/pnas.0631609100.

[6] K. Friedrich, Routes for achieving multifunctionality in reinforced polymers and composite structures, in: K. Friedrich, U. Breuer (Eds.), Multifunctionality of Polymer Composites, William Andrew Publishing, Oxford, 2015, pp. 3–41.

[7] H.W. Zhao et al., Science 375 (2022) 551–556, https://doi.org/10.1126/science.abj3343.

[8] K. Chen et al., Nat. Mater. 16 (2022) 1–9, https://doi.org/10.1038/s41563-022-01292-4.

[9] E. Munch et al., Science 322 (2008) 1516–1520, https://doi.org/10.1126/science.1164865.

[10] M. Koyama et al., Science 355 (2017) 1055–1057, https://doi.org/10.1126/science.aal2766.

[11] U.G.K. Wegst et al., Nat. Mater. 14 (2015) 23–36, https://doi.org/10.1038/nmat4089.

[12] C. Zhao et al., Science 362 (2018) eaau1925, https://doi.org/10.1126/science.aau1925.

[13] Y.Y. Zhang et al., Sci. Adv. 5 (2019) eaav5577, https://doi.org/10.1126/sciadv.aav5577.

[14] F. Peter, W. Richard, Prog. Mater Sci. 52 (2007) 1263–1334, https://doi.org/10.1016/j.pmatsci.2007.06.001.

[15] S. Deville et al., Science 311 (2006) 515–518, https://doi.org/10.1126/science.aao0185.

[16] W. Kurz, D.J. Fisher, Fundamentals of Solidification, Fourth ed., CRC Press, 1998.

[17] J.P. Qu et al., Mater. Sci. Eng. A 831 (2022), https://doi.org/10.1016/j.msea.2021.142353 142353.

[18] X. Zhu et al., J. Alloys Compd. 894 (2022), https://doi.org/10.1016/j.jallcom.2021.162284 162284.

[19] J.S. Chen et al., J. Alloys Compd. 889 (2021), https://doi.org/10.1016/j.jallcom.2021.161700 161700.

[20] Z.Y. Zhang et al., J. Mater. Sci. Technol. 48 (2020) 18–22, https://doi.org/10.1016/j.jmst.2019.12.022.

[21] N.N. Liang et al., J. Alloys Compd. 735 (2018) 1389–1394, https://doi.org/10.1016/j.jallcom.2017.11.309.

[22] Q.Z. Mao et al., Compo. Part B-Eng. 231 (2022), https://doi.org/10.1016/j.compositesb.2021.109567 109567.

[23] H. Feng et al., Mater. Sci. Eng. A 582 (2013) 219–224, https://doi.org/10.1016/j.msea.2013.06.031.

[24] W. Xu et al., Acta Mater. 225 (2022), https://doi.org/10.1016/j.actamat.2021.117607 117607.

[25] H. Li et al., Nature 604 (2022) 273–279, https://doi.org/10.1038/s41586-022-04459-w.

[26] T.H. Fang et al., Science 331 (2011) 1587–1590, https://doi.org/10.1126/science.1200177.

[27] P.J. Shi et al., Nat. Commun. 10 (2019) 489, https://doi.org/10.1038/s41467-019-08460-2.

[28] P.J. Shi et al., Mater. Today 41 (2020) 62–71, https://doi.org/10.1016/j.mattod.2020.09.029.

[29] Y.D. Wang et al., J. Mater. Sci. Technol. 288 (2021), https://doi.org/10.1016/j.jmatprotec.2020.116880 116880.

[30] G. Purcek et al., Mater. Sci. Eng. A 649 (2016) 114–122, https://doi.org/10.1016/j.msea.2015.09.111.

[31] K. Kitagawa et al., Mater. Sci. Forum 584–586 (2008) 791–796, https://doi.org/10.4028/www.scientific.net/MSF.584-586.791.

[32] L.X. Sun et al., Scr. Mater. 99 (2015) 73–76, https://doi.org/10.1016/j.scriptamat.2014.11.032.

[33] S.J. Zhang et al., Mater. Sci. Eng. A 680 (2017) 108–114, https://doi.org/10.1016/j.msea.2016.10.087.

[34] F. Han et al., Mater. Charact. 199 (2023), https://doi.org/10.1016/j.matchar.2023.112836 112836.

[35] L.J. Li et al., J. Alloys Compd. 938 (2023), https://doi.org/10.1016/j.jallcom.2022.168656 168656.

[36] J. Zha et al., Materials 16 (2023) 1592, https://doi.org/10.1016/j.msea.2017.05.114.

[37] H.F. Xie et al., J. Mater. Res. Technol. 23 (2023) 3322–3336, https://doi.org/10.1016/j.jmrt.2023.01.218.

[38] Z.X. Wu et al., Mater. Sci. Eng. A 870 (2023), https://doi.org/10.1016/j.msea.2023. 144679 144679.

[39] T.F. Dalla et al., Acta Mater. 52 (2004) 4819–4832, https://doi.org/10.1016/j.actamat.2004.06.040.

[40] Y.J. Liang et al., Nat. Commun. 4063 (2018), https://doi.org/10.1038/s41467-018-06600-8.

[41] Y.L. Zhao et al., Acta Mater. 223 (2022), https://doi.org/10.1016/j.actamat.2021.117480 117480.

[42] Y.T. Zhu, X.L. Wu, Mater. Res. Lett. 7 (2019) 393–398, https://doi.org/10.1080/21663831.2019.1616331.

[43] S.C. Xue et al., Nat. Commun. 8 (2017) 1653, https://doi.org/10.1038/s41467-017-01729-4.

[44] J. Wang et al., Appl. Phys. Lett. 95 (2009), https://doi.org/10.1063/1.3176979 021908.

[45] Q. Li et al., Adv. Mater. 30 (2018) 1704629, https://doi.org/10.1002/adma.201704629.

[46] J.H. Gao et al., Nature 590 (2021) 262–267, https://doi.org/10.1038/s41586-021-03246-3.

[47] Y. Tang et al., Prog. Mater. Sci. 135 (2023), https://doi.org/10.1016/j.pmatsci.2023.101090 101090.

[48] L. Liu et al., Science 368 (2020) 1347–1352, https://doi.org/10.1126/science.aba9413.

[49] T. Yang et al., Science 375 (2022) 647–652, https://doi.org/10.1126/science.abj9472.

[50] Z. Yin, F. Hannard, F. Barthelat, Science 364 (2019) 1260–1263, https://doi.org/10.1126/science.aaw8988.

[51] Q. Zhang et al., Nat. Commun. 11 (2020) 1–8, https://doi.org/10.1038/s41467-020-19071-7.

[52] Y.H. Zhao et al., Scr. Mater. 59 (2008) 627–630, https://doi.org/10.1016/j.scriptamat.2008.05.031.

[53] Y.H. Zhao et al., Mater. Sci. Eng. A 525 (2009) 68–77, https://doi.org/10.1016/j.msea.2009.06.031.

[54] E23 Standard Test Methods for Notched Bar Impact Testing of Metallic Materials. ASTM international, 2018.

[55] T. Ungár et al., Crystallogr. 31 (1998) 554–558, https://doi.org/10.1107/S0021889897019559.

[56] A. Arsenlis et al., Model Simul. Mater. Sci. Eng. 15 (2007) 553, https://doi.org/10.1088/0965-0393/15/6/001.
[57] M. Sudmanns et al., Addit. Manuf. 55 (2022), https://doi.org/10.1016/j.addma.2022.102791 102791.
[58] R.B. Sills et al., Fundamentals of dislocation dynamics simulations, in: C.R. Weinberger, G.J. Tucker (Eds.), Multiscale Materials Modeling for Nanomechanics, Springer Press, Switzerland, 2016, pp. 53–87.
[59] J.A. El-Awady, H.D. Fan, A.M. Hussein, Advances in discrete dislocation dynamics modeling of size-affected plasticity, in: C.R. Weinberger, G.J. Tucker (Eds.), Multiscale Materials Modeling for Nanomechanics, Springer Press, Switzerland, 2016, pp. 337–371.
[60] R.C. Reed, The Superalloys: Fundamentals and Applications, Cambridge University Press, London, 2006.
[61] J.D. Eshelby, P. R. Soc. A Math. Phy. Eng. Sci. 241 (1957) 376–396, https://doi.org/10.1098/rspa.1957.0133.
[62] J.D. Eshelby, P. R. Soc. A Math. Phys. Eng. Sci. 252 (1959) 561–569, https://doi.org/10.1098/rspa.1959.0173.
[63] A.F. Bower, Applied Mechanics of Solids, CRC Press, Boca Raton, 2009.
[64] S. Plimpton, J. Comput. Phys. 117 (1995) 1–19, https://doi.org/10.1006/jcph.1995.1039.
[65] A. Stukowski, Model. Simul. Mater. Sci. Eng. 18 (2009), https://doi.org/10.1088/0965-0393/18/1/015012 015012.
[66] O.R. Deluigi et al., Acta Mater. 213 (2021), https://doi.org/10.1016/j.actamat.2021.116951 116951.
[67] S. Li et al., Int. J. Plasticity 74 (2015) 175–191, https://doi.org/10.1016/j.ijplas.2015.05.017.